

RealSR-R1: Reinforcement Learning for Real-World Image Super-Resolution with Vision-Language Chain-of-Thought

Junbo Qiao^{1†}, Miaomiao Cai^{2†}, Wei Li^{3*}, Yutong Liu^{1,2}, Xudong Huang³,
Gaoqi He¹, Jiao Xie¹, Jie Hu³, Xinghao Chen³, Shaohui Lin^{1*}

¹East China Normal University, ² University of Science and Technology of China,
³Huawei Noah’s Ark Lab

Abstract

Real-World Image Super-Resolution is one of the most challenging task in image restoration. However, existing methods struggle with an accurate understanding of degraded image content, leading to reconstructed results that are both low-fidelity and unnatural. We present RealSR-R1 in this work, which empowers the RealSR models with understanding and reasoning capabilities. Inspired by the success of Chain of Thought (CoT) in large language models (LLMs), we simulate the human process of handling degraded images and propose the VLCoT framework, which integrates vision and language reasoning. The framework aims to precisely restore image details by progressively generating more comprehensive text and higher-resolution images. To overcome the challenge of traditional supervised learning CoT failing to generalize to real-world scenarios, we introduce, for the first time, Group Relative Policy Optimization (GRPO) into the Real-World Image Super-Resolution task. We propose VLCoT-GRPO as a solution, which designs four reward functions: (1) Format reward, used to standardize the CoT process; (2) Degradation reward, to incentivize accurate degradation estimation; (3) Understanding reward, to ensure the accuracy of the generated content; and (4) Generation reward, where we propose using a visual expert model to evaluate the quality of generated images, encouraging the model to generate more realistic images. Extensive experiments demonstrate that our proposed RealSR-R1 can generate realistic details and accurately understand image content, particularly in semantically rich scenes or images with severe degradation. Code: <https://github.com/Junboooo/RealSR-R1>.

1 Introduction

Real-world image super-resolution (RealSR) aims to reconstruct perceptually realistic high-quality (HQ) images from low-quality (LR) inputs that suffer from real-world degradations. Due to the complexity of these degradations, traditional methods [1–4] constrained by L_1 or L_2 losses may produce overly smooth outcomes, prompting many researchers to introduce GAN-based [5, 6] and diffusion-based [7–14] methods into RealSR tasks with remarkable success. However, when handling severely degraded inputs, these methods have limited ability to understand low-level image content. As shown in Fig. 1(a), they struggle to understand heavily degraded images (e.g., the roof of a dilapidated brick wall), often resulting in the generation of unnatural or implausible objects.

Recently, Multimodal Large Language Model (MLLM) leverages high-capacity networks and large-scale data training, demonstrating preliminary image understanding and generation capabilities

[†] Equal contribution.

^{*} Corresponding authors.

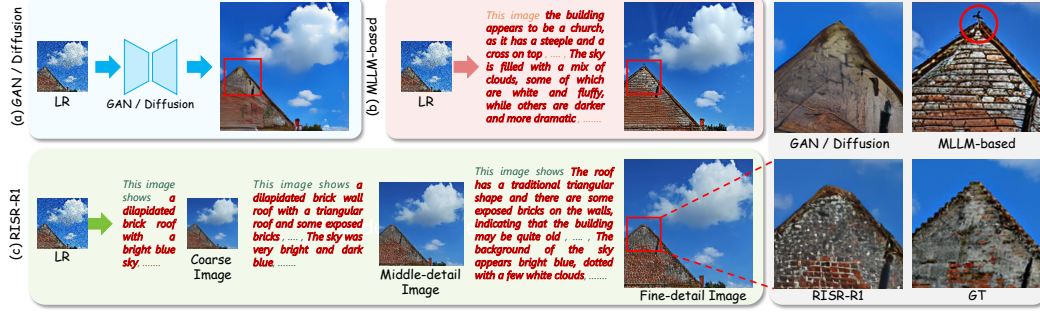


Figure 1: (a)The GAN and diffusion methods themselves do not possess the capability to understand the content of images. (b) Directly interpreting and generating detailed descriptions of degraded images leads to incorrect understanding and image restoration. (c)RealSR-R1 simulates the human image restoration process by progressively refining the understanding of image content and generating higher-quality images.

in RealSR tasks [15]. Despite the stronger understanding capabilities of such methods, directly providing detailed descriptions of severely degraded and semantically ambiguous scenarios leads to content misinterpretation and detail confusion, resulting in artifacts, random generation, or structurally inconsistent outputs. As illustrated in Fig. 1(b), the severely degraded LR depicts a scene of rooftops and sky, yet the MLLM misinterprets this scene as "the building appears to be a church, as it has a steeple and a cross on top," ultimately leading to the generation of hallucinated images.

In natural language processing (NLP) and MLLM, researchers have observed that directly mapping inputs to outputs on complex tasks often leads to biased comprehension or suboptimal outcomes [16]. Consequently, the Chain-of-Thought (CoT) mechanism [16] is proposed, guiding models to simulate the human thinking process by explicitly constructing intermediate reasoning steps. CoT significantly enhances model understanding and output reliability [17–20]. Inspired by this mechanism, we attempt to introduce CoT into RealSR to address the complex restoration problem. However, existing CoT approaches in vision typically involve intermediate reasoning processes in either pure language [21–23] or pure image [24] form. In contrast, for RealSR tasks, CoT not only requires reasoning expressed in textual form for understanding, but also needs reasoning at the visual level to accurately capture structural and perceptual details. To design a vision-language CoT process suitable for the RealSR task, we reflect on the human restoration process. We observe that it is a process where generation and understanding mutually reinforce each other, relying on extensive world priors. Specifically, humans first assess the degree of image degradation and roughly understand the image content (rather than directly jumping to pixel-level reconstruction). Then, the image is progressively restored in a coarse-to-fine manner, with a continuous deepening of understanding about the image content throughout the process.

Motivated by these insights, we propose **VLCoT**, a multi-step reasoning process that combines vision and language in a coarse-to-fine manner. As shown in Fig. 1(c), for the input LR, the model first estimates the degradation degree, coarse understanding, and coarse restored image, and then progressively generates more detailed textual understanding descriptions and higher-resolution images. Ultimately, the proposed VLCoT accurately understands the brick walls and roofs in the image and achieves the most precise image restoration.

Furthermore, we propose **VLCoT-GRPO**, which leverages Group Relative Policy Optimization (GRPO) [25] to enhance and optimize the image-text integrated reasoning process of VLCoT. We introduce reinforcement learning (RL) for two reasons: (1) Recent MLLMs have already demonstrated basic CoT reasoning capabilities in individual modalities such as text or image. To address this limitation, we aim to foster active exploration that unlocks synergistic reasoning across modalities. (2) Supervised fine-tuning (SFT) relies on imitating high-quality reasoning paths, which may lead the model to adopt "seemingly correct" patterns while failing to identify and differentiate flawed reasoning effectively. In contrast, RL encourages exploration of diverse reasoning paths, strengthens correct reasoning patterns through reward signals, and simultaneously identifies and suppresses incorrect reasoning patterns. This approach is better suited for non-regular problems like RealSR.

Unlike standard NLP tasks that typically employ clear-cut reward signals, RealSR lacks a unified, standardized reward function, posing challenges for RL-based optimization. To tackle these issues,

we propose four reward functions to comprehensively guide the VLCoT generation process: (1) Format Reward: Enforces structural conventions to ensure a well-formatted, hierarchical generation process. (2) Degradation Reward: Ensure accurate perception of degradation. (3) Understand Reward: Assesses the model’s accuracy in understanding the LR image contents, thus ensuring reasonableness and precision of the outputs. (4) Generation Reward: Using a powerful prior visual expert model, a multi-faceted evaluation of the image quality, realism and consistency of a group of outputs is provided.

Building on the aforementioned reasoning and training method, we propose **RealSR-R1**, the first reasoning-enhanced RealSR model. Experimental results demonstrate the effectiveness of our approach, and qualitative analyses further indicate that RealSR-R1 produces images more aligned with human preferences and demonstrates higher robustness when handling complex degradations or intricate scenes.

The main contributions of this paper can be summarized as follows:

- We propose **RealSR-R1**, the first reasoning-enhanced solution to the RealSR problem for more stable and trustworthy image reconstruction.
- We propose **VLCoT** that establishes a progressive, multi-step reasoning process and combines vision and language, mimicking the process of humans’ transition from understanding to image reconstruction, gradually refining the image from coarse to fine.
- We present **VLCoT-GRPO**, a reinforcement learning method for RealSR, which effectively optimizes the reasoning process of VLCoT by leveraging multiple carefully designed rewards.

2 Related Work

2.1 Real-World Image Super-Resolution.

Classical image restoration methods [2–4, 26, 27] trained with L1 or L2 loss struggle to generate high-frequency details in the Real SR task, often resulting in overly smooth outputs. Researchers have attempted to introduce GANs [5, 6, 28] into this field, but the training process is unstable, and the lack of understanding of the image content also leads to the generation of artifacts. Diffusion models have gained widespread popularity due to their strong generative capabilities. Some recent methods leverage pre-trained diffusion backbones (e.g., SD [29] or FLUX [30]) and employ ControlNet [7] and LR inputs to steer the generation process. Other methods enhance semantic alignment by leveraging additional text understanding models to extract textual descriptions [8] or class labels [10] from the LR input. One-step diffusion methods [13, 12, 11, 31, 32] direct mapping from LR to HR images with additional LoRA [33]. Despite notable improvements in perceptual quality, these approaches still struggle in complex scenarios due to limited semantic understanding, resulting in low-fidelity content representation and unnatural local structures. Recently, Wei et al. [15] introduced MLLMs into the RealSR task, significantly enhancing the model’s semantic understanding. However, unlike natural images, RealSR inputs typically suffer from severe degradation, making it challenging to directly obtain detailed and accurate image descriptions. In this paper, we propose VLCoT, a vision-language CoT framework to simulate the process of human image restoration, progressively generating detailed image content descriptions and recovering high-frequency details.

2.2 Reinforcement Learning.

The o1 [34] model proposed by OpenAI has attracted widespread attention, particularly for its advancements in enhancing reasoning capabilities through reinforcement learning (RL). DeepSeek-R1 [35] introduced a rule-based reward mechanism, Group Relative Policy Optimization (GRPO), a training paradigm that requires comprehensive reasoning before final answer generation. In recent years, this methodology has been widely adopted in the development of MLLMs [36–40] with task-specific reward functions, such as correctness [22] or IoU [41]. However, most of these tasks primarily apply reinforcement learning to pure text [21–23] or image [24, 42] inference processes. There remains a significant research gap in the RealSR tasks, which require both generation and comprehension. To address this gap, our work is the first to explore reinforcement learning for large reasoning models in the image restoration field.

3 Method

3.1 Preliminary

Group Relative Policy Optimization (GRPO) [25] is a reinforcement learning framework aimed at improving inference performance in large-scale models. In contrast to conventional approaches such as Proximal Policy Optimization (PPO) [43], which rely on an explicit value function for variance reduction, GRPO employs a baseline constructed from the mean reward of multiple rollouts conditioned on the same input. This design eliminates the dependency on auxiliary value estimation while maintaining stable and efficient policy updates. Given a question-answer pair (q, a) , a set of G responses $\{o_i\}_{i=1}^G$ is drawn from the prior policy $\pi_{\theta_{\text{old}}}$. Subsequently, the policy model $\pi_{\theta_{\text{old}}}$ is optimized by maximizing the objective function:

$$\mathcal{J}_{GRPO}(\theta) = \mathbb{E} \left[(q, a) \sim D, \{o_i\}_{i=1}^G \sim \pi_{\theta_{\text{old}}}(O | q) \right] \\ \frac{1}{G} \sum_{i=1}^G \left(\min \left(\frac{\pi_{\theta}(o_i | q)}{\pi_{\theta_{\text{old}}}(o_i | q)} A_i, \text{clip} \left(\frac{\pi_{\theta}(o_i | q)}{\pi_{\theta_{\text{old}}}(o_i | q)}, 1 - \varepsilon, 1 + \varepsilon \right) A_i \right) - \beta \mathbb{D}_{KL}(\pi_{\theta} || \pi_{\text{ref}}) \right). \quad (1)$$

GRPO adopts a clipped surrogate objective similar to that used in Proximal Policy Optimization (PPO), where ε and β are hyperparameters controlling the clipping range and regularization strength, respectively. In addition, GRPO explicitly incorporates a KL divergence penalty between the current policy π_{θ} and a reference policy π_{ref} into the loss function:

$$\mathbb{D}_{KL}(\pi_{\theta} || \pi_{\text{ref}}) = \frac{\pi_{\text{ref}}(o_i | q)}{\pi_{\theta}(o_i | q)} - \log \frac{\pi_{\text{ref}}(o_i | q)}{\pi_{\theta}(o_i | q)} - 1, \quad (2)$$

where, A_i denotes the relative advantage of the i -th response, which is obtained by feeding each sampled response into a reward model to compute its individual reward r_i . The set of rewards $\{r_1, r_2, \dots, r_G\}$ is then normalized across the group to compute the advantage values:

$$A_i = \frac{r_i - \text{mean}(\{r_1, r_2, \dots, r_G\})}{\text{std}(\{r_1, r_2, \dots, r_G\})}. \quad (3)$$

The reward functions are rule-based, evaluating the correctness of the final answer and output format without imposing constraints on the intermediate reasoning steps.

3.2 VLCoT

VLCoT process design. Unlike traditional single-modal Chain-of-Thought design, human image restoration does not separate the processes of understanding and generation. Therefore, we propose Vision-Language Chain of Thought (VLCoT), a coarse-to-fine, multi-step reasoning process that integrates both textual and visual information. As illustrated in Fig. 2, given an LR image, we guide the model to generate VLCoT reasoning with the following prompt: *‘Perceive the degradation, understand the image content, and restore the high-quality image step by step (simulating the image restoration process in three steps from coarse to fine).’* Then VLCoT decomposes the image restoration process into a sequence of multimodal reasoning steps, including: (1) degradation perception step; (2) coarse restoration step (coarse understanding and image generation); (3) middle-detail restoration step (middle-detail understanding and image generation); and (4) fine-detail restoration step (fine-detail understanding and image generation). This design mimics the human perception-to-reasoning pathway, starting from degradation awareness, followed by a coarse-to-fine process of understanding and image generation, enabling the model to progressively and robustly restore both semantic and structural information from severely degraded images.

Cold-start Initialization for VLCoT. To ensure that the model has stable output style and basic image restoration capabilities from the start, we perform cold-start training on VLCoT before fine-tuning the entire model using reinforcement learning. Specifically, we first construct paired input-output and CoT datasets, which will be detailed in the following sections, and process the concatenated text-image token sequences through autoregressive learning. Given a multimodal sequence $X = (x_1, x_2, \dots, x_T)$, where each x_t may be a text token, image patch, or other modality embedding,

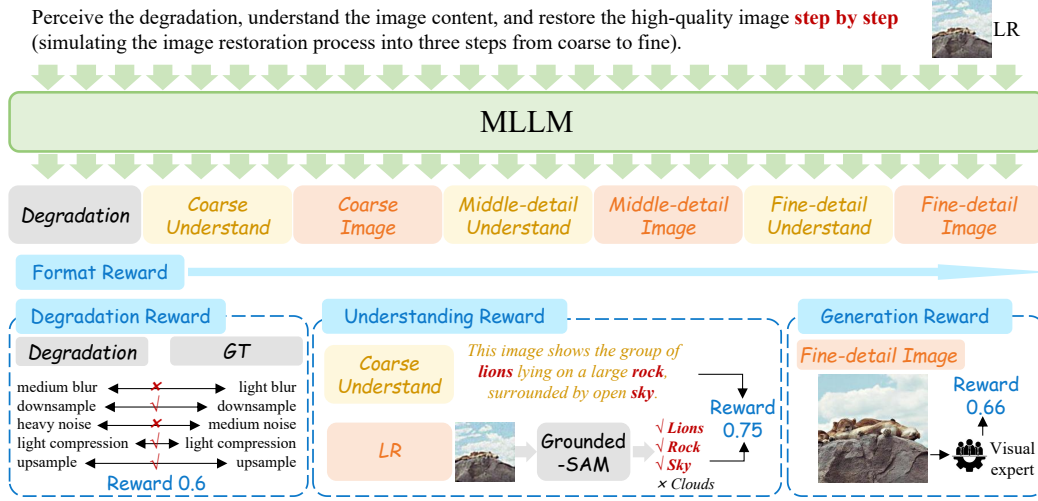


Figure 2: Illustration of the proposed RealSR-R1. The multi-step output in the center of the image represents the VLCot process. Four specially designed reward functions are displayed at the bottom, including format reward, degradation reward, understanding reward, and generation reward.

the learning objective is to maximize the likelihood of the next element conditioned on previous observations: $P_{(x|y)}(\theta) = -\sum_{t=1}^T \log P_{\theta}(x_t | x_{<t}, I)$ where I is the input and $x_{<t} = (x_1, \dots, x_{t-1})$ represents the preceding context. The overall training optimization procedure minimizes the stepwise Cross-Entropy loss between the predictions and the targets:

$$\mathcal{L} = \text{CrossEntropy}(g_t, P_{\theta}(x_t | x_{<t}, I)), \quad (4)$$

For the overall framework, we utilize Lumina-mGPT [44] as our foundation, a strong MLLM model based on a pretrained decoder-only Transformer architecture.

Degradation perception step. In the degradation perception step, we follow [6, 10] by randomly selecting degradation (e.g., Gaussian or Poisson noise) and sampling all parameters (e.g., noise intensity $\mu_1 \in [a, b]$) from a uniform distribution to determine the degradation. However, these degradation ground truth (GT) values with specific parameters are difficult for MLLMs to comprehend. Therefore, we further transform them into user-friendly summary text representations. Specifically, we follow [45, 46] to discretize the sampling distribution of the parameters for each degradation component (e.g., noise, blur, JPEG artifacts) by evenly dividing it into discrete intervals. These intervals are then discretely described and summarized to represent the degradation level. For example, we divide the distribution of noise level φ_1 into three uniform intervals, which are described as "light," "medium," and "heavy." Finally, the overall degradation representation combines the descriptions of all components, such as "[deblurring description, noise description,..., resizing description]".

Restoration step. In the image generation stage of each restoration step, the ground-truth supervision for the coarse, middle-detail, and fine-detail images is derived from the HQ image downsampled by factors of 4 and 2, as well as the original resolution, respectively. For the understanding text generation, we utilize Qwen2.5-VL [47] to produce descriptions of the GT images at each level (coarse, middle-detail, and fine-detail restoration images) through a three-round dialogue process. The detailed prompts used in the dialogue rounds are provided in the Appendix A.2.

Tokenization. For RealSR tasks, high compression ratios and limited codebook capacity result in significant information loss during the extraction of discrete image representations. To mitigate this issue, we adopt the VQGAN tokenizer from LlamaGen [48], which offers a lower downsampling factor compared to the original Lumina-mGPT (e.g., $8\times$ vs. $16\times$) and a larger visual vocabulary size (e.g., 16,536 vs. 8,192). This modification substantially reduces information loss during the encoding process, thereby improving the quality of reconstructed images in the Real-ISR task. For text tokenization, we retain the BPE tokenizer used in Lumina-mGPT, which originally has a vocabulary

size of 65,536. To accommodate the expanded image tokenizer, the BPE tokenizer’s vocabulary size is increased to 73,728, enabling it to handle a larger set of discrete image tokens.

3.3 VLCoT-GRPO

To stimulate the model’s self-exploration and enhance its reasoning ability, we propose VLCoT-GRPO. As shown in Fig. 2, VLCoT-GRPO is equipped with a set of carefully designed reward functions aimed at improving the stability and effectiveness of the multi-step, multi-modal reasoning process. Specifically, our reward R consists of four parts, including the format reward, degradation reward, understanding reward and generation reward:

$$R = R_{form} + R_{deg} + R_{und} + R_{gen} \quad (5)$$

These rewards are designed to address challenges such as inaccurate degradation perception, misunderstandings, hallucinated content, and poor restoration quality.

Format Reward. To enforce the structural integrity of the multi-step reasoning process in VLCoT, we introduce a format reward that guides the model to generate outputs with predefined tags (e.g., `<degradation>...</degradation>...`). We use rule-based checks to ensure each step is properly wrapped in corresponding tags with correct order and completeness. A reward of 1 is given for well-formed outputs; otherwise, 0.

Degradation Reward. The Degradation Reward is used to supervise the model’s output and ensure the correctness of the degradation estimation. Specifically, we compare the output with the degradation ground truth obtained from the cold-start phase degradation estimation pipeline. This comparison checks whether each discrete degradation components are correctly identified and assigns scores based on the accuracy of the degradation output. The degradation reward R_{deg} can be formalized as $R_{deg} = \frac{D_{correct}}{D_{total}}$, where $D_{correct}$ and D_{total} represent the number of correctly estimated degradations and the total number of discrete degradation components, respectively.

Understand Reward. In VLCoT, the coarse understanding plays a key role in identifying the main objects and layout of the image. Once the main objects are accurately recognized at this step, the subsequent middle- and fine-detail restoration steps can focus on detail enhancement and quality refinement based on the established coarse understanding and image. To encourage the model to build a clear and comprehensive global understanding early on, we design the Understand Reward R_{und} , which measures how well the coarse understanding text covers the main objects in the input image. Specifically, we employ Grounded-SAM [49], which supports open-vocabulary detection and segmentation, to detect main objects in the input LR images. This process extracts a set of key objects present in the scene. Subsequently, we check whether these main objects are mentioned in the coarse understanding text. If an object is explicitly referenced in the text, it is considered a hit. The Understanding Reward is defined as follows: $R_{und} = \frac{N_{cover}}{N_{total}}$, where N_{cover} denotes the number of main objects correctly mentioned in the coarse understanding text, and N_{total} represents the total number of main objects.

Generation Reward. In contrast to the rule-based reward design in GRPO, the evaluation of image restoration quality in the RealSR task typically involves multiple dimensions, including perceptual visual quality, alignment, and multi-scale structural integrity. A single predefined rule is insufficient to capture these diverse aspects. To comprehensively assess the image restoration quality, we leverage a powerful prior visual expert model (e.g., Qwen2.5-VL [47]) as a visual expert to conduct a multi-faceted evaluation of the output images, considering factors such as quality, realism, and consistency. The detailed visualization of the scoring process can be found in the Appendix A.3.

4 Experiments

4.1 Experimental Setting

Training and Testing Datasets. For cold-start stage, we adopt the full LSDIR dataset [50] and the first 10k face images from the FFHQ dataset [51] as training dataset. Then, based on Equ. 1, we select 500 high-quality images and text pairs for training our RealSR-R1. To generate the low-quality

Table 1: Quantitative comparison with state-of-the-art real-world SR methods on both synthetic and real-world benchmarks. Best and second best performance are highlighted in **red** and **blue**, respectively.

Datasets	Metrics	StableSR [52]	DiffBIR [59]	ResShift [60]	SinSR [61]	SeeSR [10]	PASD [8]	Osediff [13]	VARSR [54]	PURE [15]	RealSR-R1
OST-Val	PSNR \uparrow	20.51	20.30	20.98	20.73	20.32	20.70	20.33	20.68	17.98	18.29
	SSIM \uparrow	0.4847	0.4550	0.4930	0.4747	0.4818	0.4921	0.4760	0.4847	0.3816	0.3963
	LPIPS \downarrow	0.3825	0.3966	0.4304	0.4053	0.3569	0.4671	0.3482	0.3819	0.4664	0.4117
	DISTS \downarrow	0.2159	0.2189	0.2546	0.2305	0.2134	0.2429	0.2129	0.2351	0.2317	0.2126
	FID \downarrow	64.95	67.18	96.72	81.54	63.18	81.31	59.54	72.71	70.74	62.82
	NIQE \downarrow	4.3539	4.5481	6.0288	5.6849	4.2673	5.2597	4.2926	5.5627	4.9768	4.1504
	MUSIQ \uparrow	61.0076	69.0289	63.5278	66.2410	69.3768	56.8370	68.0248	70.3423	70.5592	71.4819
	MANIQA \uparrow	0.5886	0.6485	0.5666	0.5591	0.6527	0.5244	0.6455	0.6336	0.6547	0.6858
	CLIPQA \uparrow	0.5434	0.7012	0.6319	0.6326	0.6972	0.4769	0.6455	0.7005	0.7038	0.7127
	TOPIQ \uparrow	0.6427	0.7704	0.6893	0.7360	0.7740	0.5915	0.7602	0.7610	0.7775	0.8086
RealSR	PSNR \uparrow	24.70	24.75	26.31	26.28	25.18	25.21	25.15	22.57	22.83	22.89
	SSIM \uparrow	0.7085	0.6567	0.7421	0.7347	0.7216	0.6798	0.7341	0.7268	0.6079	0.6146
	LPIPS \downarrow	0.3018	0.3636	0.3460	0.3188	0.3009	0.3380	0.2921	0.3220	0.3821	0.3871
	DISTS \downarrow	0.2288	0.2312	0.2498	0.2353	0.2223	0.2260	0.2128	0.2356	0.2458	0.2362
	FID \downarrow	128.51	128.99	141.71	135.93	125.55	124.29	123.49	132.69	146.89	128.85
	NIQE \downarrow	5.9122	5.5346	7.2635	6.2872	5.4081	5.4137	5.6476	6.0558	5.8105	4.9399
	MUSIQ \uparrow	65.78	64.98	58.43	60.80	69.77	68.75	69.09	71.3023	66.7483	70.3638
	MANIQA \uparrow	0.6221	0.6246	0.5285	0.5385	0.6442	0.6487	0.6326	0.6541	0.6310	0.6491
	CLIPQA \uparrow	0.6178	0.6463	0.5444	0.6122	0.6612	0.6620	0.6693	0.6981	0.6817	0.7084
	TOPIQ \uparrow	0.6809	0.7313	0.6242	0.6411	0.7354	0.5988	0.7106	0.7422	0.7165	0.7371
RealLR250	NIQE \downarrow	4.5282	4.7524	5.3275	5.1777	4.4451	4.3240	4.4181	5.2372	4.7158	4.0454
	MANIQA \uparrow	67.3269	71.7762	65.7151	66.8540	70.3724	65.8979	70.9796	73.8639	72.6105	73.4231
	MUSIQ \uparrow	0.6352	0.6686	0.5753	0.5825	0.5927	0.6142	0.6478	0.6704	0.6886	0.6601
	CLIPQA \uparrow	0.6566	0.7667	0.6336	0.6781	0.7062	0.6183	0.7097	0.7556	0.7753	0.7813
	TOPIQ \uparrow	0.6893	0.7629	0.6795	0.7084	0.6939	0.6572	0.7286	0.7653	0.7781	0.7884

(LR) images, we employ the degradation process of Real-ESRGAN [6] and use the same degradation settings as in SeeSR [10] to ensure a fair comparison. For testing datasets, following previous works [52–54, 13], we use three real-world datasets and one synthetic dataset for evaluation. For the real-world datasets, we test on the Dreal [55] and real [56] testset provided by Osediff [13], as well as the RealLR250 [57] dataset. Due to space limitations, the results of Dreal can be found in the Appendix A.5. Following PURE [15], we use the OST-Val [58] dataset, processed with the same degradation process in SeeSR [10], as the synthetic test set.

Metrics. To comprehensively evaluate the performance of different methods, we combine full-reference and no-reference metrics. PSNR and SSIM [62] (calculated on the Y channel in the YCbCr color space) are full-reference fidelity measures, while LPIPS [63] and DISTS [64] are full-reference perceptual quality metrics. FID [65] assesses the distributional distance between the original and reconstructed images. For blind quality assessment of no-reference images, we combine NIQE [66], MANIQA [67], MUSIQ [68], CLIPQA [69], and TOPIQ [70] to evaluate the naturalness and structural integrity of the images.

Implementation Details. In the cold-start phase, we use the AdamW optimizer with an initial learning rate of 2×10^{-5} , and employ a cosine annealing strategy for learning rate decay. The model is trained for 2 epochs on the entire dataset with batchsize=16, including a warmup phase spanning the first 0.01 epochs to stabilize early-step optimization. In the VLCoT-GRPO phase, the AdamW optimizer is again used with an initial learning rate of 1×10^{-5} , a batch size of 8, and a constraint on the maximum generated token length of $6k$. For the same LR image, RealSR-R1 samples three responses and provides corresponding rewards. The model was trained for 2 epochs. The experiments are performed on 16 NVIDIA A100 GPUs.

4.2 Comparison with State-of-the-Arts

Quantitative Comparisons. The quantitative comparison is shown in Tab. 1. On synthetic datasets, RealSR-R1 achieves the best or second-best results across seven metrics, reflecting the capability to generate high-quality and realistic images. On real-world benchmarks, our method performs strongly across most no-reference metrics and shows comparable performance to diffusion-based methods on reference-based metrics. However, PSNR and SSIM still have a gap with diffusion-based methods. This is due to the trade-off between realism and fidelity, as RealSR-R1 generates more textures and details, which may reduce fidelity metrics. Recent studies [71, 9, 57] have shown that the restored images exhibit higher quality in terms of human perception, but perform poorly on certain reference-based metrics (e.g., PSNR and SSIM). Therefore, it is necessary to reconsider the reference

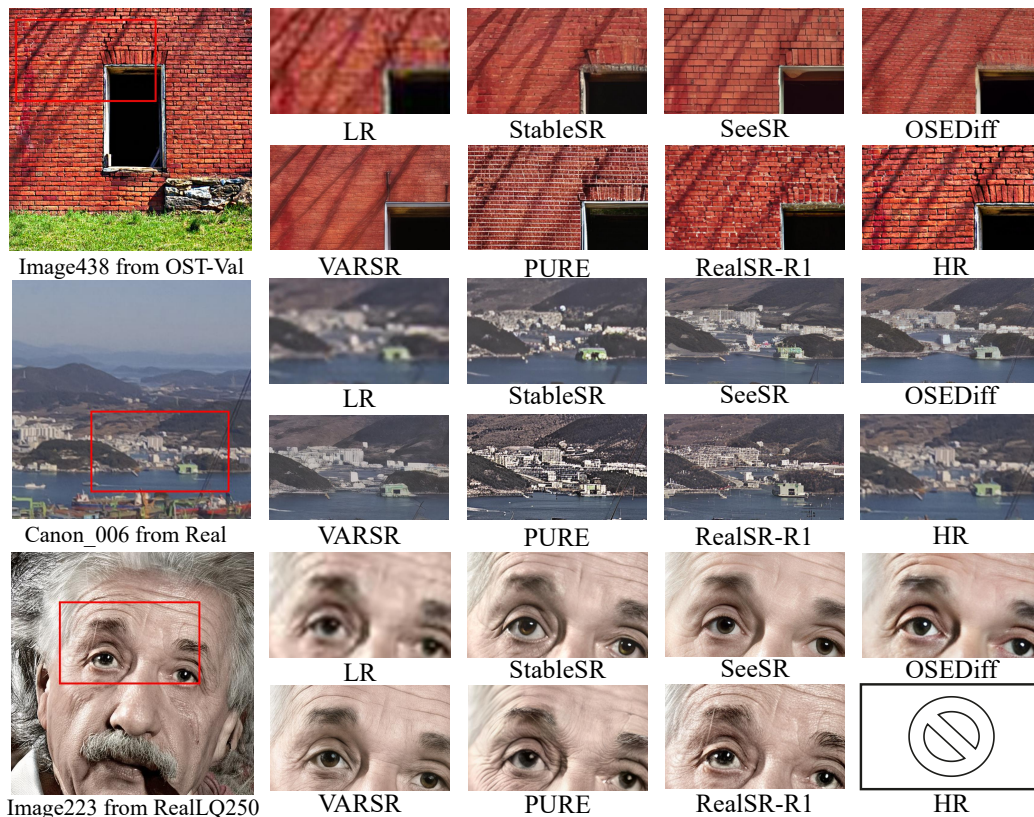


Figure 3: Qualitative comparisons with different SOTA methods.

values of existing metrics and propose more effective methods to evaluate modern image restoration methods.

Qualitative Comparisons. In Fig. 3, we present a visual comparison of different datasets. As shown in the first case, even when faced with severely degraded input, RealSR-R1 generates realistic wall texture details, while other methods produce overly smooth or incorrect textures. In the second example, SeeSR and OSediff produce blurred structures in the background buildings, while PURE introduces excessive pseudo-textures. In contrast, our method most accurately restores the image details. On the RealLR250 dataset, RealSR-R1 also demonstrates an advantage in visual quality, generating more realistic face details while maintaining better overall image fidelity. Additional visual comparison results and the complete CoT output are provided in the Appendix A.4.

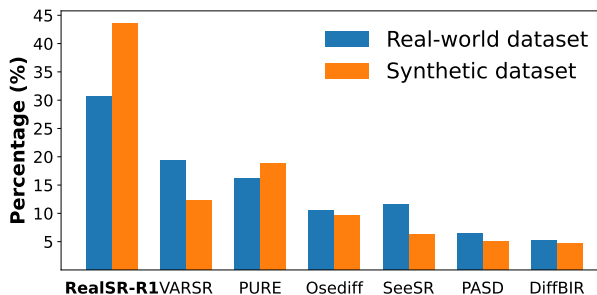


Figure 4: User study results on real-world dataset and synthetic dataset.

User Study. To further demonstrate that the images generated by our method align more closely with human perception, we conducted a user study with 20 participants, evaluating both synthetic and real-world data. Specifically, we randomly selected 50 real-world LR images from RealSR, DrealSR, and RealLR250, and chose 25 degraded images from the synthetic dataset OST-Val. We then compared the enhancement results of RealSR-R1 with six methods (PURE, SeeSR, StableSR, PASD, DiffBIR, and OSediff). Participants were asked to vote on the best restoration results based on visual quality, naturalness, and accuracy. As shown in Fig. 4, our RealSR-R1 achieved better



	GAN	Diffusion	MLLM	RealSR-R1
	None	animal, bear, brown, brown bear, floor, food, grass, grassy, green, lush, stand, walk	...The image features a small brown rabbit standing in a grassy field , surrounded by tall grass. The rabbit appears to be looking at the camera. ... the viewer's attention. The field is filled with various plants, creating a lush and natural environment for the rabbit brown animal is in image. The background consists of green foliage and grass ... The image show a raccoon as...The raccoon's fur is thick and textured ... The animal appears to be foraging The raccoon 's face is marked by its iconic black ...with its head lowered towards the ground...The colors range from deep forest green to lighter, almost yellow-green hues...
	None	clock, bell tower, building, church, mountain, tower, spire	...which is situated in a mountainous area ... The building itself has a distinctive architectural style, with a combination of stone and brick elements ...The overall atmosphere of the image is one of grandeur and historical significance , showcasing the impressive architecture and the breathtaking natural landscape...	Two tall, gray stone towers ... foreground ... A mountain range forms the backgroundThe left tower features an arched opening with visible bells ... a cluster of buildings with terracotta roofsThe texture of the stone is rough and weathered ...in color ranging from light gray to darker ... The background... its slopes covered in earthy tones and patches of green vegetation ...

Figure 5: Comparison of the understanding ability of different methods on real SR tasks.

Table 2: Ablation of the VLCot on OST-Val.

Method	OST-Val				
	SSIM↑	LPIPS↓	MANIQA↑	CLIPQA↑	TOPIQ↑
RealSR-R1	0.3963	0.4117	0.6858	0.7127	0.8086
-VLCot GRPO	0.3792	0.4481	0.6735	0.7096	0.7859
-Degradation output	0.3564	0.4618	0.6651	0.6993	0.7876
-Understanding output	0.3512	0.4593	0.6408	0.6819	0.7784
-Multi output	0.3359	0.4875	0.6267	0.6715	0.7547

Table 3: Ablation on reward functions.

Reward	OST-Val				
	SSIM↑	LPIPS↓	MANIQA↑	CLIPQA↑	TOPIQ↑
RealSR-R1	0.3963	0.4117	0.6858	0.7127	0.8086
-Understanding	0.3874	0.4353	0.6804	0.7089	0.8024
-Degradation	0.3765	0.4649	0.6833	0.7101	0.8015
-Generation	0.3816	0.4432	0.6798	0.7055	0.7831

preferences across different datasets than other methods, with a selection rate of 30.7% and 43.6%, respectively. This result demonstrates its advantage in generating high-quality images.

Understanding Capabilities of Different Models We further compared the understanding capabilities of GAN-based, Diffusion-based, and MLLM-based methods for real image super-resolution. As shown in Fig. 5, GAN-based methods lack an understanding of image content, while diffusion-based methods utilize external language models (e.g., DAPE [10]) to extract simple image descriptions as prompts. MLLMs possess more refined understanding capabilities, but directly applying this fine-grained understanding to severely degraded images leads to incorrect interpretations of details. For example, diffusion and MLLM mistakenly interpret the image as a bear and a rabbit, respectively. In contrast, only RealSR-R1 correctly recognizes the image as a raccoon and generates the most accurate and detailed image description, which is crucial for restoring image details.

4.3 Ablation Study

Ablation of the key components of RealSR-R1. To validate the effectiveness of RealSR-R1, we systematically conducted ablation experiments on OST-Val. We progressively removed core components from RealSR-R1. The results, as shown in Tab 2, removing the VLCot GRPO leads to significant reductions in all metrics, demonstrating the substantial potential of R1 in real-world super-resolution. Secondly, the degradation and understanding output affect different metrics: removing the degradation output and removing the understanding output significantly reduce the reference-based metrics SSIM, LPIPS, and the no-reference metric MANIQA, respectively. Furthermore, removing multi-step outputs and reducing the length of CoT performs poorly on most metrics. These observations validate the effectiveness of each core component of the proposed method.

Ablation of VLCot-GRPO and reward functions. We further performed a step-by-step removal of the proposed reward functions to ablate their effectiveness. In Tab. 3, we find that different rewards affect different metrics. For example, the generation reward significantly improves CLIPQA and TOPIQ, while the degradation reward tends to improve SSIM and LPIPS. Additionally, removing the understanding reward impacts image restoration quality across all metrics, indicating that semantic understanding plays a crucial role in driving the generation of real-world details.

5 Conclusion and Limitation

In this paper, we propose a novel reinforcement Learning method for the real-world image super-resolution (RealSR) task, named RealSR-R1. The proposed Visual-Language Chain of Thought (VLCoT) framework effectively integrates vision and language, simulating human-like reasoning in image restoration, progressively refining low-resolution images into high-quality outputs. Furthermore, we propose VLCoT-GRPO and design reward functions to guide the model to ensure accurate degradation estimation, robust understanding, and precise generation of high-quality images. Extensive experiments and user studies demonstrate that RealSR-R1 outperforms existing state-of-the-art methods, achieving higher perceptual quality while maintaining alignment with human perception.

While our results are promising, we acknowledge that RealSR-R1 has some limitations. Our model relies on synthetic degradation ground truth (GT) as supervision for the degradation reward during training; however, GT for real-world images is often difficult to obtain. In future work, we will further investigate how to eliminate the need for GT images during training.

References

- [1] Dong, C., C. C. Loy, K. He, et al. Learning a deep convolutional network for image super-resolution. In *Computer Vision—ECCV 2014: 13th European Conference, Zurich, Switzerland, September 6–12, 2014, Proceedings, Part IV 13*, pages 184–199. Springer, 2014. 1
- [2] Liang, J., J. Cao, G. Sun, et al. Swinir: Image restoration using swin transformer. In *ICCV*, pages 1833–1844. 2021. 3
- [3] Lim, B., S. Son, H. Kim, et al. Enhanced deep residual networks for single image super-resolution. In *Proceedings of the IEEE conference on computer vision and pattern recognition workshops*, pages 136–144. 2017.
- [4] Zhang, Y., K. Li, K. Li, et al. Image super-resolution using very deep residual channel attention networks. In *Proceedings of the ECCV (ECCV)*, pages 286–301. 2018. 1, 3
- [5] Ledig, C., L. Theis, F. Huszár, et al. Photo-realistic single image super-resolution using a generative adversarial network. In *Proceedings of the IEEE conference on computer vision and pattern recognition*, pages 4681–4690. 2017. 1, 3
- [6] Wang, X., L. Xie, C. Dong, et al. Real-esrgan: Training real-world blind super-resolution with pure synthetic data. In *ICCV*, pages 1905–1914. 2021. 1, 3, 5, 7
- [7] Zhang, L., A. Rao, M. Agrawala. Adding conditional control to text-to-image diffusion models. In *ICCV*, pages 3836–3847. 2023. 1, 3
- [8] Yang, T., R. Wu, P. Ren, et al. Pixel-aware stable diffusion for realistic image super-resolution and personalized stylization. In *ECCV*, pages 74–91. Springer, 2024. 3, 7, 15
- [9] Yu, F., J. Gu, Z. Li, et al. Scaling up to excellence: Practicing model scaling for photo-realistic image restoration in the wild. In *CVPR*, pages 25669–25680. 2024. 7
- [10] Wu, R., T. Yang, L. Sun, et al. Seesr: Towards semantics-aware real-world image super-resolution. In *CVPR*, pages 25456–25467. 2024. 3, 5, 7, 9, 15
- [11] Chen, B., G. Li, R. Wu, et al. Adversarial diffusion compression for real-world image super-resolution. *arXiv preprint arXiv:2411.13383*, 2024. 3
- [12] Sun, L., R. Wu, Z. Ma, et al. Pixel-level and semantic-level adjustable super-resolution: A dual-lora approach. *arXiv preprint arXiv:2412.03017*, 2024. 3
- [13] Wu, R., L. Sun, Z. Ma, et al. One-step effective diffusion network for real-world image super-resolution. *NeurIPS*, 37:92529–92553, 2024. 3, 7, 15
- [14] Cheng, K., L. Yu, Z. Tu, et al. Effective diffusion transformer architecture for image super-resolution. In *AAAI*, vol. 39, pages 2455–2463. 2025. 1

- [15] Wei, H., S. Liu, C. Yuan, et al. Perceive, understand and restore: Real-world image super-resolution with autoregressive multimodal generative models. *arXiv preprint arXiv:2503.11073*, 2025. 2, 3, 7, 15
- [16] Wei, J., X. Wang, D. Schuurmans, et al. Chain-of-thought prompting elicits reasoning in large language models. *NeurIPS*, 35:24824–24837, 2022. 2
- [17] Yao, S., D. Yu, J. Zhao, et al. Tree of thoughts: Deliberate problem solving with large language models. *NeurIPS*, 36:11809–11822, 2023. 2
- [18] Mondal, D., S. Modi, S. Panda, et al. Kam-cot: Knowledge augmented multimodal chain-of-thoughts reasoning. In *AAAI*, vol. 38, pages 18798–18806. 2024.
- [19] Mu, Y., Q. Zhang, M. Hu, et al. Embodiedgpt: Vision-language pre-training via embodied chain of thought. *NeurIPS*, 36:25081–25094, 2023.
- [20] Zhang, Z., A. Zhang, M. Li, et al. Multimodal chain-of-thought reasoning in language models. *arXiv preprint arXiv:2302.00923*, 2023. 2
- [21] Shao, H., S. Qian, H. Xiao, et al. Visual cot: Advancing multi-modal language models with a comprehensive dataset and benchmark for chain-of-thought reasoning. *NeurIPS*, 37:8612–8642, 2024. 2, 3
- [22] Liu, Z., Z. Sun, Y. Zang, et al. Visual-rft: Visual reinforcement fine-tuning. *arXiv preprint arXiv:2503.01785*, 2025. 3
- [23] Pan, J., C. Liu, J. Wu, et al. Medvlm-r1: Incentivizing medical reasoning capability of vision-language models (vlms) via reinforcement learning. *arXiv preprint arXiv:2502.19634*, 2025. 2, 3
- [24] Guo, Z., R. Zhang, C. Tong, et al. Can we generate images with cot? let’s verify and reinforce image generation step by step. *arXiv preprint arXiv:2501.13926*, 2025. 2, 3
- [25] Shao, Z., P. Wang, Q. Zhu, et al. Deepseekmath: Pushing the limits of mathematical reasoning in open language models. *arXiv preprint arXiv:2402.03300*, 2024. 2, 4
- [26] Qiao, J., W. Li, H. Xie, et al. Lipt: Latency-aware image processing transformer. *IEEE Transactions on Image Processing*, 2025. 3
- [27] Qiao, J., J. Liao, W. Li, et al. Hi-mamba: Hierarchical mamba for efficient image super-resolution. *arXiv preprint arXiv:2410.10140*, 2024. 3
- [28] Qiao, J., S. Lin, Y. Zhang, et al. Dcs-risr: Dynamic channel splitting for efficient real-world image super-resolution. *Neural Networks*, 184:107119, 2025. 3
- [29] Stability.ai. <https://stability.ai/stable-diffusion>. 3
- [30] Labs, B. F. Flux. <https://github.com/black-forest-labs/flux>, 2024. 3
- [31] He, X., H. Tang, Z. Tu, et al. One step diffusion-based super-resolution with time-aware distillation. *arXiv preprint arXiv:2408.07476*, 2024. 3
- [32] Wu, X., J. Xin, Z. Tu, et al. One-step diffusion-based real-world image super-resolution with visual perception distillation. *arXiv preprint arXiv:2506.02605*, 2025. 3
- [33] Hu, E. J., Y. Shen, P. Wallis, et al. Lora: Low-rank adaptation of large language models. *ICLR*, 1(2):3, 2022. 3
- [34] Jaech, A., A. Kalai, A. Lerer, et al. Openai o1 system card. *arXiv preprint arXiv:2412.16720*, 2024. 3
- [35] Guo, D., D. Yang, H. Zhang, et al. Deepseek-r1: Incentivizing reasoning capability in llms via reinforcement learning. *arXiv preprint arXiv:2501.12948*, 2025. 3
- [36] Chen, L., L. Li, H. Zhao, et al. Vinci,“r1-v: Reinforcing super generalization ability in vision-language models with less than \$3,” 2025, accessed: 2025-02-02. 3

- [37] Meng, F., L. Du, Z. Liu, et al. Mm-eureka: Exploring visual aha moment with rule-based large-scale reinforcement learning. *arXiv preprint arXiv:2503.07365*, 2025.
- [38] Yang, Y., X. He, H. Pan, et al. R1-onevision: Advancing generalized multimodal reasoning through cross-modal formalization. *arXiv preprint arXiv:2503.10615*, 2025.
- [39] Zhang, J., J. Huang, H. Yao, et al. R1-vl: Learning to reason with multimodal large language models via step-wise group relative policy optimization. *arXiv preprint arXiv:2503.12937*, 2025.
- [40] Deng, Y., H. Bansal, F. Yin, et al. Openvlthinker: An early exploration to complex vision-language reasoning via iterative self-improvement. *arXiv preprint arXiv:2503.17352*, 2025. [3](#)
- [41] Liu, Y., B. Peng, Z. Zhong, et al. Seg-zero: Reasoning-chain guided segmentation via cognitive reinforcement. *arXiv preprint arXiv:2503.06520*, 2025. [3](#)
- [42] Cai, M., S. Li, W. Li, et al. Dspo: Direct semantic preference optimization for real-world image super-resolution. *arXiv preprint arXiv:2504.15176*, 2025. [3](#)
- [43] Schulman, J., F. Wolski, P. Dhariwal, et al. Proximal policy optimization algorithms. *arXiv preprint arXiv:1707.06347*, 2017. [4](#)
- [44] Liu, D., S. Zhao, L. Zhuo, et al. Lumina-mgpt: Illuminate flexible photorealistic text-to-image generation with multimodal generative pretraining. *arXiv preprint arXiv:2408.02657*, 2024. [5](#)
- [45] Zhang, R., J. Gu, H. Chen, et al. Crafting training degradation distribution for the accuracy-generalization trade-off in real-world super-resolution. In *ICML*, pages 41078–41091. PMLR, 2023. [5](#)
- [46] Chen, Z., Y. Zhang, J. Gu, et al. Image super-resolution with text prompt diffusion. *arXiv preprint arXiv:2311.14282*, 2023. [5](#)
- [47] Bai, S., K. Chen, X. Liu, et al. Qwen2. 5-vl technical report. *arXiv preprint arXiv:2502.13923*, 2025. [5](#), [6](#), [14](#)
- [48] Sun, P., Y. Jiang, S. Chen, et al. Autoregressive model beats diffusion: Llama for scalable image generation. *arXiv preprint arXiv:2406.06525*, 2024. [5](#)
- [49] Ren, T., S. Liu, A. Zeng, et al. Grounded sam: Assembling open-world models for diverse visual tasks. *arXiv preprint arXiv:2401.14159*, 2024. [6](#)
- [50] Li, Y., K. Zhang, J. Liang, et al. Lsdir: A large scale dataset for image restoration. In *CVPR*, pages 1775–1787. 2023. [6](#)
- [51] Karras, T., S. Laine, T. Aila. A style-based generator architecture for generative adversarial networks. In *CVPR*, pages 4401–4410. 2019. [6](#)
- [52] Wang, J., Z. Yue, S. Zhou, et al. Exploiting diffusion prior for real-world image super-resolution. *International Journal of Computer Vision*, 132(12):5929–5949, 2024. [7](#), [15](#)
- [53] Dong, L., Q. Fan, Y. Guo, et al. Tsd-sr: One-step diffusion with target score distillation for real-world image super-resolution. *arXiv preprint arXiv:2411.18263*, 2024.
- [54] Qu, Y., K. Yuan, J. Hao, et al. Visual autoregressive modeling for image super-resolution. *arXiv preprint arXiv:2501.18993*, 2025. [7](#), [15](#)
- [55] Wei, P., Z. Xie, H. Lu, et al. Component divide-and-conquer for real-world image super-resolution. In *Computer Vision–ECCV 2020: 16th European Conference, Glasgow, UK, August 23–28, 2020, Proceedings, Part VIII 16*, pages 101–117. Springer, 2020. [7](#)
- [56] Cai, J., H. Zeng, H. Yong, et al. Toward real-world single image super-resolution: A new benchmark and a new model. In *ICCV*, pages 3086–3095. 2019. [7](#)

- [57] Ai, Y., X. Zhou, H. Huang, et al. Dreamclear: High-capacity real-world image restoration with privacy-safe dataset curation. *NeurIPS*, 37:55443–55469, 2024. 7
- [58] Wang, X., K. Yu, C. Dong, et al. Recovering realistic texture in image super-resolution by deep spatial feature transform. In *Proceedings of the IEEE conference on computer vision and pattern recognition*, pages 606–615. 2018. 7
- [59] Lin, X., J. He, Z. Chen, et al. Diffbir: Toward blind image restoration with generative diffusion prior. In *ECCV*, pages 430–448. Springer, 2024. 7, 15
- [60] Yue, Z., J. Wang, C. C. Loy. Resshift: Efficient diffusion model for image super-resolution by residual shifting. *NeurIPS*, 36:13294–13307, 2023. 7, 15
- [61] Wang, Y., W. Yang, X. Chen, et al. Sinsr: diffusion-based image super-resolution in a single step. In *CVPR*, pages 25796–25805. 2024. 7, 15
- [62] Wang, Z., A. C. Bovik, H. R. Sheikh, et al. Image quality assessment: from error visibility to structural similarity. *IEEE transactions on image processing*, 13(4):600–612, 2004. 7
- [63] Zhang, R., P. Isola, A. A. Efros, et al. The unreasonable effectiveness of deep features as a perceptual metric. In *Proceedings of the IEEE conference on computer vision and pattern recognition*, pages 586–595. 2018. 7
- [64] Ding, K., K. Ma, S. Wang, et al. Image quality assessment: Unifying structure and texture similarity. *IEEE transactions on pattern analysis and machine intelligence*, 44(5):2567–2581, 2020. 7
- [65] Heusel, M., H. Ramsauer, T. Unterthiner, et al. Gans trained by a two time-scale update rule converge to a local nash equilibrium. *NeurIPS*, 30, 2017. 7
- [66] Zhang, L., L. Zhang, A. C. Bovik. A feature-enriched completely blind image quality evaluator. *IEEE Transactions on Image Processing*, 24(8):2579–2591, 2015. 7, 15
- [67] Yang, S., T. Wu, S. Shi, et al. Maniqa: Multi-dimension attention network for no-reference image quality assessment. In *CVPR*, pages 1191–1200. 2022. 7, 15
- [68] Ke, J., Q. Wang, Y. Wang, et al. Musiq: Multi-scale image quality transformer. In *ICCV*, pages 5148–5157. 2021. 7, 15
- [69] Wang, J., K. C. Chan, C. C. Loy. Exploring clip for assessing the look and feel of images. In *AAAI*, vol. 37, pages 2555–2563. 2023. 7, 15
- [70] Chen, C., J. Mo, J. Hou, et al. Topiq: A top-down approach from semantics to distortions for image quality assessment. *IEEE Transactions on Image Processing*, 2024. 7, 15
- [71] You, Z., Z. Li, J. Gu, et al. Depicting beyond scores: Advancing image quality assessment through multi-modal language models. In *ECCV*, pages 259–276. Springer, 2024. 7
- [72] Zhang, Y., X. Huang, J. Ma, et al. Recognize anything: A strong image tagging model. In *CVPR*, pages 1724–1732. 2024. 14

A Appendix

A.1 More Ablations

The ablation of understanding reward. We conduct ablation studies on tag extraction strategies within the understanding reward to evaluate the impact of different tag extraction methods on model performance. As shown in Tab 4, RAM [72] performs poorly on both perceptual and generative metrics, which may be attributed to the fact that the extracted tags often contain incorrect or misleading information. In contrast, the tags extracted by Ground-SAM achieve the best performance across all four metrics. Therefore, we adopt Ground-SAM as the tag extraction method for the understanding reward in RealSR-R1.

Table 4: Ablation of tag extraction strategies within the Understanding reward.

Method	SSIM↑	LPIPS↓	OST-Val		
			MANIQA↑	CLIPQA↑	TOPIQ↑
RAM	0.3847	0.4226	0.6759	0.7065	0.8019
Qwen2.5-VL	0.4023	0.4136	0.6813	0.7082	0.8032
Ground-SAM	0.3963	0.4117	0.6858	0.7127	0.8086

The ablation of generation reward. We also conduct ablation studies on the visual expert used in the generation reward. As shown in Tab. 5, employing either perceptual metrics or generative metrics as the visual expert significantly enhances the corresponding perceptual or generative quality—while simultaneously degrading performance on the other. In contrast, Qwen2.5-VL achieves the best trade-off between these two objectives. Therefore, we adopt Qwen2.5-VL as the visual expert in RealSR-R1 to score generated images. It is also worth noting that using hand-crafted metrics involves evaluating each score independently, whereas Qwen2.5-VL can jointly assess the perceptual and generative quality of a given image set, leading to more holistic and context-aware scoring. Visualization of the scoring process is provided in Sec A.3.

Table 5: Ablation of the generation reward. The perceptual metric is computed as a weighted combination of PSNR, SSIM, LPIPS, and DISTS scores, while the generative quality metric is defined as a weighted aggregation of CLIPQA, MANIQA, MUSIQ, and TOPIQ scores.

Method	SSIM↑	LPIPS↓	OST-Val		
			MANIQA↑	CLIPQA↑	TOPIQ↑
Perceptual metrics	0.4298	0.3672	0.6578	0.6849	0.7633
Generate metrics	0.3595	0.4781	0.6869	0.7106	0.8168
Qwen2.5-VL	0.3963	0.4117	0.6858	0.7127	0.8086

A.2 The Detailed Prompts Used in the Dialogue.

we leverage Qwen2.5-VL [47] to generate ground-truth supervision for textual understanding at coarse, middle, and fine levels—required during the cold-start stage. As illustrated in Fig. 6, we employ a three-round dialog process, where progressively detailed image descriptions are generated through prompt-based interaction. Each round is guided by specifically designed prompts to elicit increasingly fine-grained textual understanding of the visual content.

A.3 Scoring Process for Generating Rewards.

Fig. 7 illustrates the scoring process of generated images using a powerful prior visual expert model (e.g., Qwen2.5-VL [47]). The expert conducts a multi-faceted evaluation of each output image, taking into account factors such as quality, realism, and consistency. Alongside the individual scores, the expert provides interpretability through rationale for each assessment. Finally, the scores across all dimensions are aggregated via a weighted sum to produce an overall image quality score.

A.4 Visualization of the Complete VLCoT Output.

We further visualize the full image and text output process of VLCoT. As shown in Fig. 8, RealSR-R1 progressively generates multi-level textual understanding and multi-resolution image outputs, which serve as intermediate "gray" reasoning steps. This step-by-step process ultimately leads to an accurate reconstruction of the target image.

A.5 More Extensive Quantitative Results.

We further report comparative results between RealSR-R1 and state-of-the-art RealSR models on the DReal dataset. As shown in Tab 6, RealSR-R1 achieves superior performance across multiple generative metrics (e.g., NIQE [66], MANIQA [67], MUSIQ [68], CLIPQA [69], and TOPIQ [70]), demonstrating its strong ability to generate more realistic images. It is worth noting that although VARSR achieves competitive performance in image generation, its training relies on proprietary data. In contrast, RealSR-R1 surpasses VARSR in generation metrics while being trained solely on publicly available datasets.

Table 6: Quantitative comparison with state-of-the-art real-world SR methods on both synthetic and real-world benchmarks. Best and second best performance are highlighted in **red** and **blue**, respectively.

Datasets	Metrics	StableSR [52]	DiffBIR [59]	ResShift [60]	SinSR [61]	SeeSR [10]	PASD [8]	Osediff [13]	VARSR [54]	PURE [15]	RealSR-R1
DrealSR	PSNR \uparrow	28.03	26.71	28.46	28.36	28.17	27.36	27.92	28.15	24.39	24.61
	SSIM \uparrow	0.7536	0.6571	0.7673	0.7515	0.7691	0.7073	0.7835	0.7654	0.6084	0.5797
	LPIPS \downarrow	0.3284	0.4557	0.4006	0.3665	0.3189	0.3760	0.2968	0.3540	0.4615	0.4861
	DISTS \downarrow	0.2269	0.2748	0.2656	0.2485	0.2315	0.2531	0.2165	0.2525	0.2756	0.2803
	FID \downarrow	148.98	166.79	172.26	170.57	147.39	156.13	135.30	157.59	174.16	171.56
	NIQE \downarrow	6.5239	6.3124	8.1249	6.9907	6.3967	5.5474	6.4902	6.8709	6.3894	5.8207
	MUSIQ \uparrow	58.51	61.07	50.60	55.33	64.93	64.87	64.65	68.0896	63.24	64.9527
	MANIQA \uparrow	0.5601	0.5930	0.4586	0.4884	0.6042	0.6169	0.5899	0.5961	0.5924	0.6188
	CLIPQA \uparrow	0.6356	0.6395	0.5342	0.6383	0.6804	0.6808	0.6963	0.7196	0.6789	0.7241
	TOPIQ \uparrow	0.6208	0.6899	0.5646	0.6211	0.7026	0.6398	0.6758	0.7302	0.7121	0.7319

A.6 More Visualization Results.

We add more visualization results of our RealSR-R1, making comparisons with other SOTA methods on different datasets. As shown in Fig.9 and Fig.10, RealSR-R1 achieves superior performance in scenes involving human faces, animal fur, architectural structures, and plant textures, yielding results that are more consistent with human perceptual preferences.

Text Understanding Dialogue Example



Based on the input image, generate a rough description that includes only the overall layout and basic structure. Specifically, describe the main elements in the image (such as the main subject, background, and foreground). Keep it around 50 words.



A vast golden field takes over the foreground. The middle contains hills and greenery. The background shows a gradual sky, transitioning from a warm orange near the horizon to a cooler hue above, and faint clouds.



Building on the description from the previous round, generate a moderately detailed description based on the input image. Emphasize significant features and enhance local details. Specifically, add descriptions of the main subject's prominent characteristics. Include some texture, shadows, and color variations to make the scene appear more three-dimensional. Maintain overall consistency while highlighting areas with clearer detail. Note that correct any errors from the previous description if needed.



This image captures the serene countryside at sunset. The foreground is occupied by a large golden wheat field whose texture ripples with subtle shadows cast by the setting sun. There is a row of dark, leafy trees on the middle ground. Beyond the trees, rolling hills stretch into the distance. The background is a stunning gradient sky, transitioning from deep orange near the horizon to more subdued hues above, with slender clouds adding to the ethereal atmosphere.



Based on the descriptions from the previous two rounds, generate a highly detailed description based on the input image, adding fine details for a realistic effect. Specifically, include descriptions of the minute features of the main subject. Emphasize light-shadow interaction, color gradients, and subtle textures to make the image look more realistic. Include small details in the background that may have been overlooked. Correct errors from the previous description if needed.



The image depicts a breathtaking view of a rural sunset. In the foreground is a vast field of golden wheat, with straws swaying gently and gleaming in the warm light of the setting sun. The fine shadows cast by the undulating terrain add dimension. On the ground in the middle, a row of dark, foliage trees stands as a natural border. Their shadows stretch across the ground. Beyond the trees, rolling hills extend into the distance, their outlines softened by the dim light. The hills take on a gradient of color, from a dark green closer to the viewer to a softer blue hue further away. Small fields and possibly hordes of buildings nestle among the hills against a stunning sky painted in warm color gradients in the background. Near the horizon, the sky emits a deep orange hue, gradually transitioning to softer yellows and pinks as it rises. Thin clouds scattered across the sky.

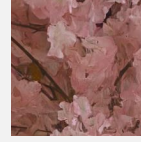
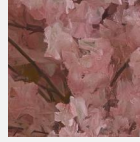
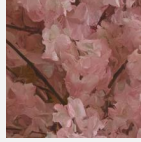


Figure 6: Visual example of step-by-step generation of detailed image descriptions.

Generation Reward Example



Please rate the last three restored images based on the quality of the input image in terms of quality, realism, and consistency. Use a score from 0 (worst) to 1 (best) for each image. The first image is the input.



Quality: 0.8

- The overall image is clear and details are well preserved.
- Color saturation and contrast are moderate, and the visuals are good.

Realism: 0.7

- The texture and light effect of the petals are realistic.
- However, the details in some areas are slightly blurred, which is slightly different from the real image.

Consistency: 0.8

- High consistency in color and composition with the original image.
- The details are close to the original.

Overall rating: 0.77

Quality: 0.6

- The overall image is blurry and details are lost.
- Color saturation is low and appears a little dull.

Realism: 0.5

- The texture and light effect of the petals are not clear enough and appear unnatural.
- The details in some areas are rough.

Consistency: 0.7

- There is a certain similarity to the original in color and composition.
- But the details vary greatly and the consistency is average.

Overall rating: 0.60

Quality: 0.7

- The image has moderate clarity and complete detail retention.
- Color saturation and contrast are reasonable.

Realism: 0.6

- The texture and light effects of the petals are realistic, but there is still room for improvement.
- The details in some areas are not fine enough.

Consistency: 0.8

- High consistency in color and composition with the original image.
- Close to the original in detail, but slightly different in some areas.

Overall rating: 0.70



Therefore, the final score is: [0.77, 0.60, 0.70]

Generation Reward Example



Please rate the last three restored images based on the quality of the input image in terms of quality, realism, and consistency. Use a score from 0 (worst) to 1 (best) for each image. The first image is the input.



Quality: 0.7

- The overall image is clear, and details such as the texture of the building and the clouds of the sky are well restored.
- Color saturation is moderate, but slightly overexposed compared to the original image.

Realism: 0.75

- The scale and structure of the building looks natural and matches the actual scene.
- Light and shadow effects are properly handled to enhance the realism of the image.

Consistency: 0.8

- Consistency of major features (e.g. outlines of towers and buildings) compared to the first input image.
- The restoration of details is accurate, but some parts (such as the details of the ground) are slightly different.

Overall rating: 0.75

Quality: 0.6

- The overall clarity of the image is slightly less than that of the second one, and the details are slightly blurred.
- High color saturation, causing some areas to appear unnatural.

Realism: 0.65

- The structure and proportion of the building are basically reasonable, but the light and shadow effect is not as natural as the second one.
- The details of some areas (such as ground and trees) are not fine enough.

Consistency: 0.7

- The main features are consistent compared to the first input image.
- But there is a lack of detail restoration (such as the texture of the building and the complexity of the ground).

Overall rating: 0.65

Quality: 0.8

- The overall clarity of the image is high and the details are rich, the texture of the buildings and the clouds of the sky are very clear.
- Color saturation is moderate and the overall tone is harmonious.

Realism: 0.85

- The scale and structure of the building are very natural, and the light and shadow effects are handled very well, enhancing the realism of the image.
- The ground and trees are also finely detailed, adding depth to the scene.

Consistency: 0.85

- Major features and details are well restored compared to the first input image.
- The overall style and atmosphere are highly consistent with the input image, with little noticeable difference.

Overall rating: 0.83



Therefore, the final score is: [0.75, 0.65, 0.83]

Figure 7: Illustrative example of a vision expert model assigning scores to a set of images.

Complete VLoT Output Example



User

Perceive the degradation, understand the image content, and restore the high-quality image step by step (simulating the image restoration process from coarse to fine). The low-quality image is as follows: `<image|>`.


The generation format should be as follows: `<degradation> ... </degradation> <coarse_understand> ... </coarse_understand> <coarse_image> ... </coarse_image> <middle_understand> ... </middle_understand> <middle_image> ... </middle_image> <final_understand> ... </final_understand> <final_image> ... </final_image>`

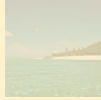


`<degradation>` medium blur, downsample, medium noise, medium compression, upsample `</degradation>`



RealSR-R1

`<coarse_understand>` The image is a coastal scene with sand in the foreground. The background includes a tree-lined hill and clear blue sky with clouds be in attractive disorder `</coarse_understand>` `<coarse_image>`  `</coarse_image>`

`<middle_understand>` In the foreground of this image is a sandy beach, which appears smooth and light in color, in contrast to the vibrant waters. In the background, a lush green hill rises up, dotted with trees casting subtle shadows. The sky is gorgeous blue and dotted with soft and fluffy white clouds, adding a sense of tranquility. `</middle_understand>` `<middle_image>`  `</middle_image>`


`<final_understand>` The image depicts serene coastal views. In the foreground, the sand stretches out, with a smooth, pale beige surface, and a subtle texture due to the gentle rise and fall of the tides. The water near the shore transitions to a deeper green as it extends towards the horizon. The gentle waves gleamed in the sun. The texture of the water is dynamic. Lighter areas on the water reflect sunlight, and darker patches indicate deeper areas in the water. In the background is a lush green hill. The vegetation on the mountain is dense, and the greens of different shades represent different types of plants and trees. The leaves appear thick and vibrant, casting long shadows on the hillside. Above the hill, the sky was blue, almost cloudless, with only a few white clouds scattered on it. The color of the sky is bright blue. `</final_understand>` `<final_image>`  `</final_image>`

Figure 8: Visual example of VLoT’s complete image and text output process.

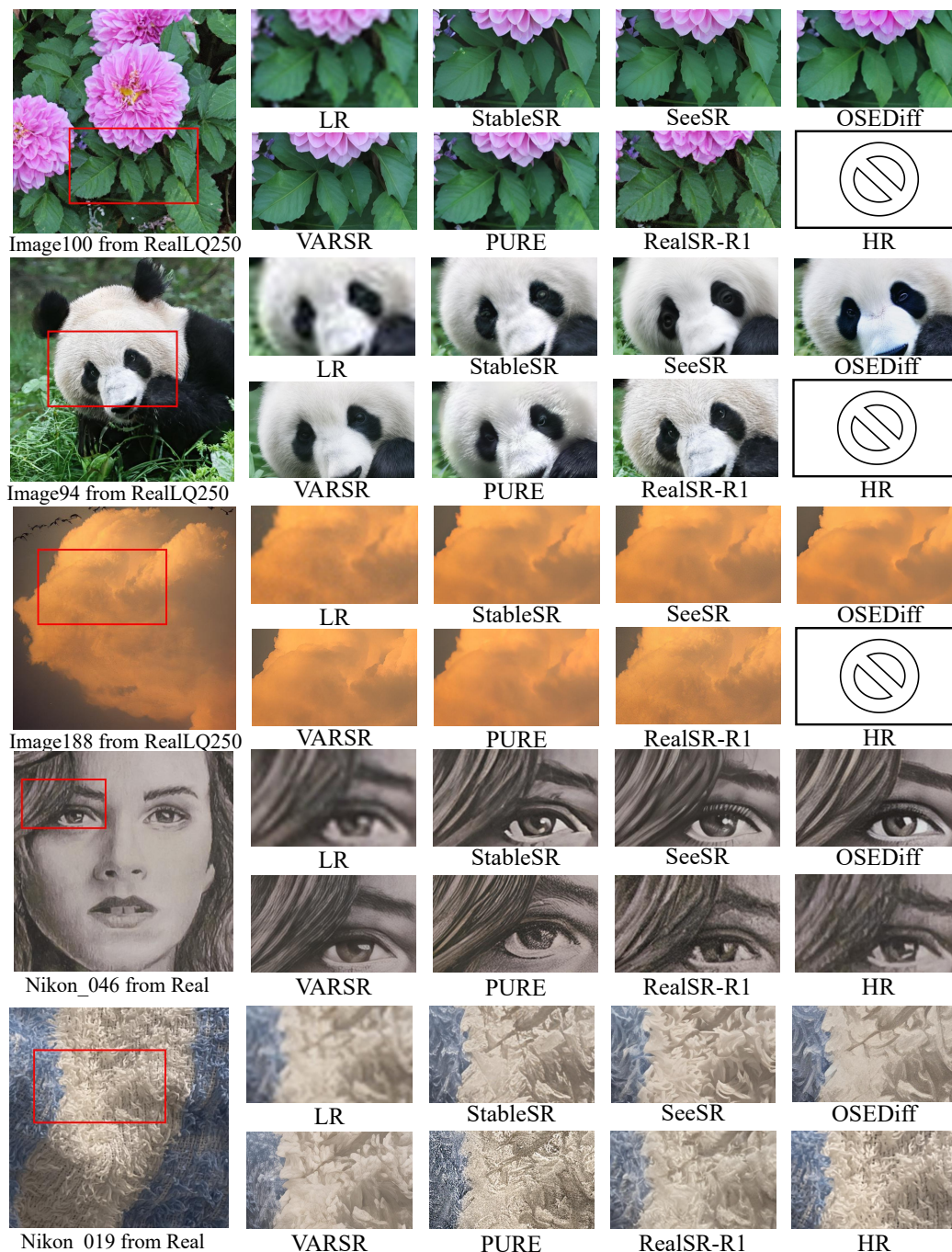


Figure 9: Qualitative comparisons with different SOTA methods.

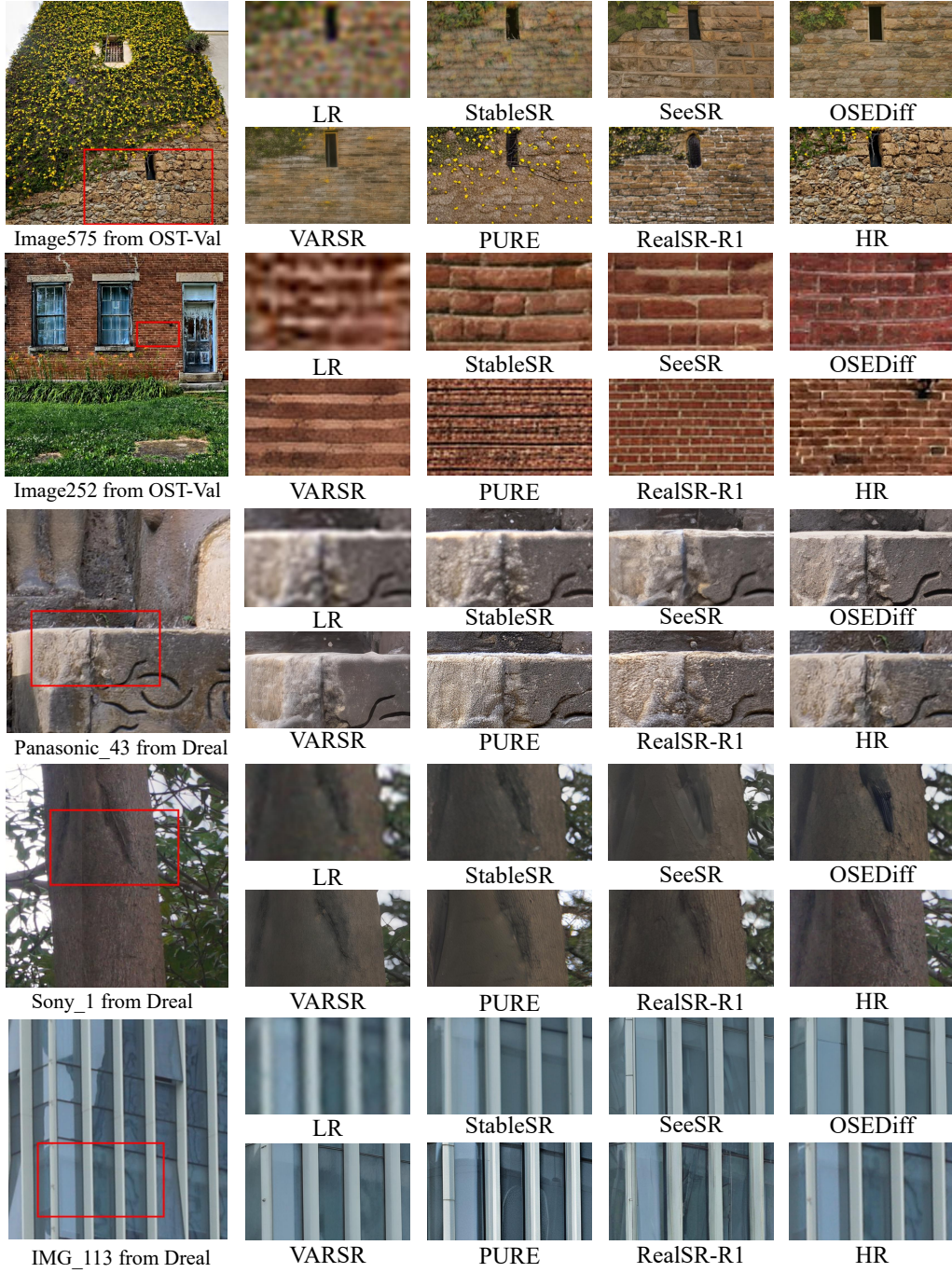


Figure 10: Qualitative comparisons with different SOTA methods.